Received: 18 February 2018 | Revised: 15 May 2018 | Accepted: 6 June 2018
DOI: 10.1002/we.2226

RESEARCH ARTICLE

WILEY

Improving the efficiency of wind farms via wake manipulation

Shujaut Bader | Venkatesh Inguva | J. B. Perot

Theoretical and Computational Fluid Dynamics Laboratory, Department of Mechanical and Industrial Engineering, University of Massachusetts Amherst, Amherst, Massachusetts 01003, USA

Correspondence
J. B. Perot, Theoretical and Computational Fluid Dynamics Laboratory, Department of Mechanical and Industrial Engineering, University of Massachusetts Amherst, Amherst, Massachusetts 01003, USA.
Email: perot@ecs.umass.edu

Funding information
National Science Foundation, Grant/Award Numbers: 1336502 and 1353942

Abstract

Wind turbine farms suffer from wake losses, where the downstream turbines generate less power, and/or the leading turbines are throttled to reduce the downstream power losses. In this paper, we focus on possible external modifications that can enhance the wind turbines' performance when they are operating in a farm environment. In particular, this study is interested in enhancing the performance of the downstream turbines in wind farms. The idea is to move each turbine's wake down and away from subsequent turbines. This goal is achieved by using stationary external airfoils that are placed in proximity to the rotating blades. A number of different designs are tested and the design concepts are tested using Reynolds-Averaged Navier-Stokes simulations of an aligned array of 2 wind turbines. The turbines are modeled as actuator disks with axial induction and are placed in a velocity field that is modeled as a turbulent atmospheric boundary layer. It is found that fixed external airfoils can enable partial or full power recovery at turbine separations of as small as 3 rotor diameters downstream. We will also demonstrate that some devices can also improve the performance of the upstream turbine. The physical reasons for these power recovery phenomena are discussed.

KEYWORDS

efficiency, turbine, wake, Wind Ring

1 | INTRODUCTION

The role of renewable and nonconventional sources of energy is expected to be of prime importance in the future. The concern for environmental conservation and sustainability has strongly shifted the attention of world's energy leaders from fossil fuels to the nonconventional energy resources. One of the promising candidates in the renewable energy sector is wind energy technology. Advanced blade manufacturing and optimized blade aerodynamics together with novel design considerations remain critical to the efficient use of the wind resource and continued growth of wind technology. In 2008, the US Department of Energy published a report that examines the technical feasibility of using wind energy to generate 20% of the nation's electricity demand by 2030.[1]

In this paper, we pursue an enhancement not mentioned in the Department of Energy report, which is the control and displacement of wind turbine wakes. Modern day wind farms often consist of a large number of individual turbines arranged in a group or cluster with an interturbine spacing of 6 to 10 rotor diameters. The leading (or upstream) turbine in an array is the one to receive the fastest air. After it extracts a part of the energy from the incoming wind stream, it creates a wind shade in the region behind it, which is referred to as the wake. As a result, the wind behind the leading wind turbine is energy deficient and more turbulent than the wind flowing into the turbine. Hence, in large wind farms consisting of many rows of turbines, the wakes generated by upstream turbines are often incident upon the downstream turbines (see Figure 1). The interaction of the wakes with the downstream turbines reduce the power output of the downstream turbine significantly. The average power loss due to wind turbine wakes is 10% to 20% of the total power output in large offshore wind farms.[2]

The power available in the wind is proportional to the cube of its speed. A small increase/decrease in the speed of the wind can increase/decrease the power associated with it by a large amount. This is why small improvements in the wake location and strength can have an oversized

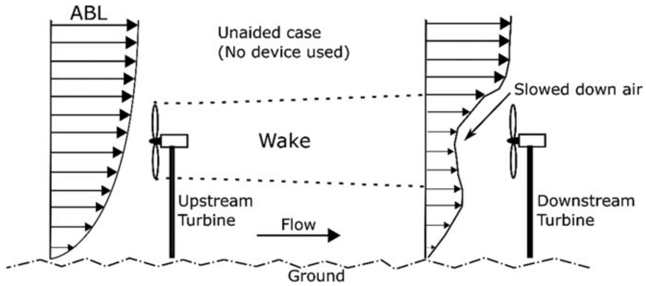

FIGURE 1 Illustration of a wind turbine wake incident upon the downstream turbine

effect on the downstream turbine's power output. The prime objective of the work presented in this paper is to relocate the wake and facilitate the velocity recovery via controlling the wake flow by employing the proposed devices appropriately around or in the vicinity of the upstream turbine (refer Figure 2).

The proposed work is novel. However, it is loosely related to vertical velocity entrainment in windfarms, which has been more extensively studied. In the atmosphere, air speed typically increases with altitude (as shown in Figures 1 and 2). Wind turbine performance can therefore be enhanced if the high speed air above the turbines can be brought down to the turbine level. This is usually done by mixing the air to cause some of the high speed air to move downwards, and this is called vertical entrainment. Our devices also perform some vertical entrainment as a side effect, but they are much more concerned with altering the wake of the upstream turbine than in influencing the air input to the downstream turbine.

Several experiments and simulations have focused on the concept of wake steering via turbine yaw to improve the wind turbine array efficiency.[3-8] Yaw sends the wake sideways rather than down. One of the most thoroughly studied technique is the active control of wakes by intentional yaw misalignment of the upwind turbines. Schottler et al[3] have experimentally investigated the wake deflection potential of 2 different model wind turbines in yaw and reported the skew angles (defined as the angle of the actual flow leaving the turbine and the rotor axis) in the range of $3 - 3.8^{\circ}$. Gebraad et al,[7,8] based on their studies of combined layout optimization and wake steering control, have reported an increase of 5% in the annual energy production of Princess Amalia Wind Park in Netherlands. Furthermore, these studies mention that with fully optimized layout with yaw, the reduction in wake losses went up to 31.4% from that of the optimized but nonyawed condition in which the reduction of wake losses was reported to be only about 8.8% compared with the baseline configuration of nonoptimized layout with zero-yaw. Thus, wake control by yawing an upwind turbine has the potential to reduce the wake losses. In our work, the wake deflection uses a passive device and the devices will be able to reduce the wake losses entirely. As a side effect, these devices also have the potential to improve the upwind turbine's efficiency too.

Various experiments and simulations have shown the vertical kinetic energy entrainment can be of the same order of magnitude as the total energy extracted by the turbines.[9,10] A few attempts have been tried at the enhancement of the vertical transport of energy via hypothetical or real mixing devices. VerHulst and Charles Meneveau[11] used large eddy simulation of the turbulent atmospheric boundary layer (ABL) flow over wind turbines and applied a hypothetical synthetic forcing to the flow at the turbine rotor locations. It was shown that this improved the power generation from the wind farm, and the total extracted power increase was about 24% for the array of 4 wind turbines placed in tandem with a spacing of 6 rotor diameters. Based on these studies,[9-11] researchers at Delft University of Technology conducted a large eddy simulation study of a wind turbine array with tethered kites that create turbulence and enhance vertical mixing.[12]

In addition, a variety of diffuser shrouded wind turbines have been devised to improve the collection and acceleration of the wind through the wind turbine rotor. The shrouded wind turbine designs like the diffuser augmented wind turbines and the wind lens are purely an attempt to improve the performance of a single wind turbine.[13-16] We mention them only because some of our designs superficially look similar to these shrouded systems. However, despite their looks, the function, physics, and purpose of our devices is entirely different. Shrouds are intended to increase the airflow input through the turbine rotor that they shroud. Our devices are intended to divert the turbine “exhaust” stream so that it does not hit downstream turbines.

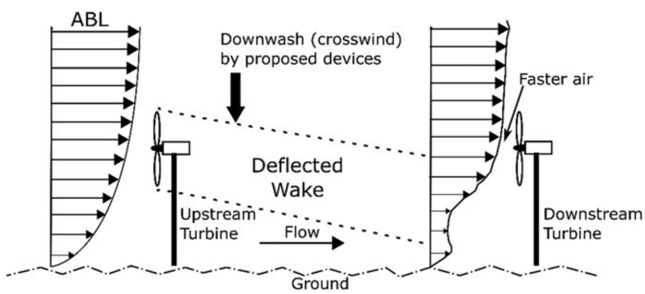

FIGURE 2 Illustration of velocity recovery and wake displacement in a wind turbine using proposed devices

2 | NUMERICAL SETUP AND FORMULATION

2.1 | Computational domain

This study consists of numerous simulations of a pair of wind turbines aligned in a row and modeled as actuator discs with axial induction to account for the energy extracted by each turbine. Table 1 summarizes all the geometrical parameters along with their dimensions for both the domain sizes. Figure 3 represents these parameters marked on the computational domain.

2.2 | Governing equations

In this research, 3-dimensional Reynolds-Averaged Navier-Stokes (RANS)[17] simulations of an aligned array of 2 wind turbines are solved using the Opensource Field Operation and Manipulation (OpenFOAM)[18] software. The effects being studied in this work are largely due to external geometry, so an actuator disk model was deemed sufficient. Detailed RANS simulations of the rotating blades and their trailing vortices have been performed elsewhere but are not required here.[19] The governing equations are

$$\begin{aligned} \frac{\partial \overline{u}_i}{\partial t}+\overline{u}_j\frac{\partial \overline{u}_i}{\partial x_j} &= -\frac{1}{\rho}\frac{\partial \overline{p}}{\partial x_i}+\frac{\partial}{\partial x_j}\nu\frac{\partial \overline{u}_i}{\partial x_j}+\frac{\partial\left(\overline{\acute{u}_i\ \acute{u}_j}\right)}{\partial x_j}+\frac{1}{\rho}f_i \\ \frac{\partial \overline{u}_i}{\partial x_i} &= 0, \end{aligned} \tag{1}$$

where x_i represents the position, $\overline{u}_i$ the mean flow velocity in i-direction, $\overline{p}$ the averaged pressure, and f_i the body force per unit volume acting on the fluid (in particular, this is the axial force in the regions of the actuator disks that mimics drag from the wind turbine). The properties ρ and ν are the density and kinematic viscosity of the fluid. The turbulent viscosity comes from the solution of the k/omega Shear Stress Transport (SST) turbulence model (see Section 2.6). The left-hand side of the first equation above represents the change in mean momentum of the fluid element while the right-hand side consists of the contributions of various forces that balance this change. For clarity, the terms (in order) on the right-hand side represent the isotropic stress owing to the mean pressure field, the viscous stresses, the apparent stresses (or Reynolds' stresses) owing to the fluctuating velocity field and as already mentioned the last term represents the mean body force per unit volume that the turbine causes in the actuator disk. The second equation is the incompressibility constraint.

A customized subroutine was written in C++ using OpenFOAM to model the turbines as actuator discs with axial induction. A large time-step transient solver for incompressible flow called *pimpleFoam*, which is essentially based on a merged PISO-SIMPLE algorithm implemented in OpenFOAM, was used.[17,20] The motivation behind our choice of the solver is that we can use larger Courant numbers (Co > > 1), and therefore, the time step can be increased to reduce the run time.

TABLE 1 Dimensions of 2 different computational domains

Parameter	Small Domain Values, m	Large Domain Values, m
D	50	50
S	150	300
h	75	75
L	350	500
W	200	200
H	200	200

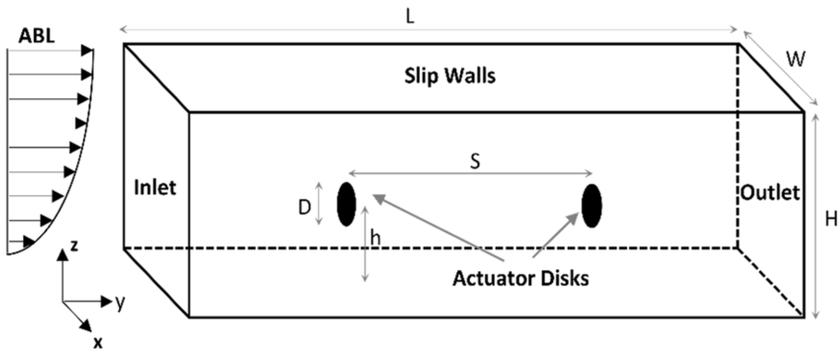

FIGURE 3 Computational domain showing inlet, outlet, and walls with proper representation of dimensions (not to scale)

2.3 | Rotor modeling

It is known that the thrust acting on a wind turbine can be modeled via the actuator disk method as follows[21]:

$$T = 2\rho AU^2 a(1-a), \tag{2}$$

where ρ = density of air (kg/m^3), A = blade plane (rotor) area (m^2), U = upstream wind speed (m/s), and $a = \frac{U-U_{rotor}}{U}$ is the perturbation factor. From the definition of the perturbation factor, it follows that

$$U_{rotor} = U(1-a), \tag{3}$$

where U_{rotor} is the wind speed at the rotor plane.

From the above discussion, the drag force in terms of the wind speed at the rotor can be modeled as follows:

$$f = 2\rho U_{rotor}^2 \frac{A}{V}\frac{a}{1-a}, \tag{4}$$

where f is the force per unit volume and V is the total actuator disc volume. This equation has been used for the drag force inside each actuator disk. The actuator disks are imparted with a force in the axial direction only. The effects of rotation on the streamwise velocity at distances larger than 3 diameters downstream are reported as being negligible by Gomes et al,[22] and one simulation (not presented) confirmed this result.

The values of the perturbation factor "a" are chosen according to the desired coefficient of performance (C_p) values using the equation $C_p = 4a(1-a)^2$. The beauty of Equation (4) is that it provides an easy way to translate the C_p value to the corresponding axial force or thrust acting on the wind turbine. Our results consider device performance with 2 different C_p values of 0.45 and 0.50.

2.4 | Discretization

The meshing of the flow domain was performed by using ANSYS ICEM, which is a commercial software package used for CAD and mesh generation.[23] We have used an unstructured tetrahedral mesh in all the simulations. Figure 4 illustrates the mesh density used in this study. The cell count used in all the simulations was in the range of 2.5 to 3 million cells. The parts of mesh in the immediate vicinity of the proposed devices are meshed using prism layers to capture the physics of boundary layer effectively. We have avoided extremely small $y+$ values, primarily because the complete resolution of the boundary layer is not necessary for the present project, since only the wind deflection potential of the proposed devices is of interest. The zones of the mesh that act as actuator discs are modeled as 5-m-thick cylindrical cell sets with an axial force applied opposite to the flow. The generated mesh is converted into a suitable format that can be read by OpenFOAM solver. For the successful execution of the simulation, accuracy of the results and stability of the solver, the largest aspect ratio of the tetrahedra and the population of skewed cells was minimized. A backward Euler time-stepping method was employed to approach the steady-state solution rapidly.[24]

2.5 | Boundary conditions

The inlet boundary of the flow domain is set to a nonuniform boundary condition, which mimics the logarithmic wind profile of the ABL as shown below,

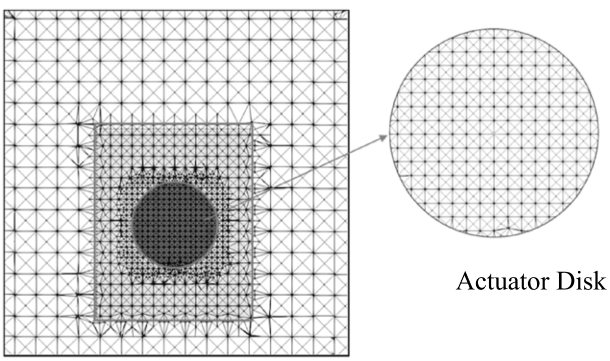

FIGURE 4 A vertical cut through one of the actuator disks illustrating the mesh density used in the study

$$U(z) = \frac{u^*}{\kappa}\ln\left(\frac{z-d}{z_0}\right). \tag{5}$$

For the application of interest, $z^+ = \frac{zu^*}{\nu} > 45$, and formula (5) holds. The variable u^* is the friction (or shear) velocity (=0.62 m/s) and is determined so that a reference velocity of 10 m/s is found at the centerline of the turbines (at 75 m altitude), κ is the Von Karman constant (=0.41), d is the zero-plane displacement (=0.666 m), and z_0 is the surface roughness (=0.1 m). The values of zero-plane displacement and surface roughness are based on the average height of roughness elements, which we have set equal to 1 m in our case. Figure 5 shows the vertical logarithmic velocity profile that has been used as the inlet velocity profile in our simulations.

The nonuniform boundary condition, which mimics the logarithmic wind profile, was coded using a built-in library *groovyBC* in OpenFOAM. The boundary conditions for the other boundaries are summarized in Table 2.

2.6 | Turbulence modeling

The k-ω SST turbulence model, which is a 2 equation model for the turbulence kinetic energy, k, and turbulence frequency, ω, was used to solve for the turbulent eddy viscosity in our simulations.[25] The use of the k-ω formulation in the inner parts of the boundary layer makes the model directly usable all the way down to the wall through the viscous sublayer, similar to the turbulent potential model.[26] The SST formulation also switches to a k-ε behavior in the free-stream and thereby avoids the common k-ω problem that the model is too sensitive to the inlet free-stream turbulence properties. The SST k-ω model is implemented in OpenFOAM as follows. [27] In this model, the turbulent frequency and turbulent kinetic energy are given by the following equations, respectively:

$$\begin{aligned} \frac{D}{Dt}(\rho\omega) &= \nabla\cdot\ (\rho D_\omega \nabla\omega) + \frac{\rho\gamma G}{\nu} - \frac{2}{3}\rho\gamma\omega(\nabla\cdot\mathbf{u}) - \rho\beta\omega^2 - \rho\,(F_1 - 1)CD_{k\omega} + S_\omega \\ \frac{D}{Dt}(\rho k) &= \nabla\cdot(\rho D_k \nabla k) + \rho G - \frac{2}{3}\rho k(\nabla\cdot\mathbf{u}) - \rho\beta^*\omega k + S_k. \end{aligned} \tag{6}$$

The turbulent viscosity is obtained by using the following formula:

$$\nu_t = a_1 \frac{k}{\max(a_1\omega, b_1 F_{23}\mathbf{S})}. \tag{7}$$

The model variables, namely, k and ω are initialized as per the following formulae ((8)) and ((9)):

$$k = \frac{3}{2}(I|\mathbf{u_{ref}}|)^2, \tag{8}$$

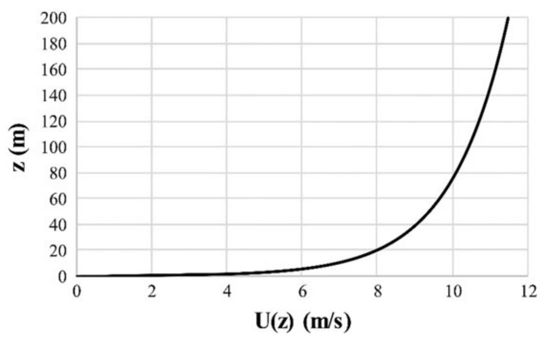

FIGURE 5 Vertical log profile of inlet velocity

TABLE 2 Boundary conditions for velocity and pressure

Boundary Patch	Velocity BC	Pressure BC
Inlet	*groovyBC* (ABL inlet)	zeroGradient
Outlet	zeroGradient	fixedValue = 0
Side walls	Slip	zeroGradient
Device surface	No slip	zeroGradient

Abbreviation: ABL, atmospheric boundary layer.

where I is the turbulence intensity, and $\mathbf{u_{ref}}$ a reference velocity (10 m/s in our simulations). Also, the reference length scale is computed as follows:

$$L = \frac{k^{0.5}}{C_\mu \omega} \tag{9}$$

where the constant C_μ = 0.09. More details about the implementation of this model in OpenFOAM can be found in (Menter et al[28]). Resolving the viscous sublayer of a boundary layer is computationally expensive, so the wall function approach, which relies on the law-of-the-wall assumption, was used. In OpenFOAM, the wall functions are ordinary boundary conditions that are applied to boundary patches of type wall. The boundary conditions, which are required for variables ν_t, k, and ω, are summarized in Table 3.

3 | DEVICE GEOMETRY

The airfoil profile used to generate the wake-modifier designs is a NACA 2412.[29] The chord length of all the designs is 10 m and the maximum thickness at 30% of the chord from the leading edge is 1.2 m, which translates to 12% of the chord length. In this section, the geometry of each device will be presented below:

Device 1: This is the most basic design of all. In this case, a NACA 2412 airfoil having a span of 50 m and a chord of 10 m is placed 5 m above upstream actuator disk (AD-1) at 13° angle of attack, as shown in Figure 6A.

Device 2: In this case, a NACA 2412 airfoil having a span of 50 m and a chord of 10 m is placed 5 m below AD-1 at 17° angle of attack, as shown in Figure 6B.

Device 3: In this case, 2 NACA 2412 airfoils having a span of 50 m and a chord of 10 m are placed 5 m above and below AD-1 at 13° and 17° angle of attack, respectively (see Figure 6C).

Device 4: In this case, 2 NACA 2412 airfoils having a span of 50 m and a chord of 10 m are placed 5 m on either sides of AD-1 at 17° angle of attack (see Figure 6D).

Device 5: In this case, 2 NACA 2412 airfoils having span of 50 m and chord of 10 m are placed at 13° above AD-1. As evident from Figure 6E, the airfoils are placed such that the arrangement improves the magnitude of total downwash generated.

Device 6: In this case, 3 NACA 2412 airfoils having span of 50 m and chord of 10 m are placed at 13°, 13°, and 15° angle of attack, 30 m behind AD-1. The airfoils are separated by 10 m from each other. As evident from Figure 6F, the airfoils are placed such that the arrangement deflects the wake from the upstream turbine downwards.

Device 7: This device consists of a curved airfoil placed above AD-1. The geometry of this device is generated by driving the NACA 2412 profile along an arc of radius 30 m, length 50 m, and subtending a central angle of 95° (approx) at the center of AD-1. The angle with the horizontal is maintained at 13° everywhere along the device. Refer Figure 6G.

Device 8: This design consists of a curved device placed below AD-1. The geometry is generated by driving the NACA 2412 profile along a semi-circular arc of radius 30 m. As the whole device lies below the horizontal mid-plane of the rotor, the angle with the horizontal has been relaxed to 17° everywhere along the device. Refer Figure 6H.

Device 9: This device is a combination of Devices 7 and 8. Refer Figure 6I.

Device 10: This design is a modification of Device 9. The upper and lower curved airfoils are joined together to form a closed ring-like device around the rotor. For its resemblance to a ring, it has been given the name "Wind Ring." Refer Figure 6J.

At the Reynolds number relevant to these devices the NACA 2412 airfoil stalls at an angle of about 15°. The flow field behind the actuator disk is an expanding streamtube, which means that the incoming wind is incident upon the leading edge of an airfoil at different angles, depending upon where the airfoil is located. If the airfoil is located above the horizontal mid-plane of the rotor, the flow comes in at a positive angle of attack, by a few degrees, as compared with the flow unaltered by the presence of rotor. Similarly, if the airfoil is located below the horizontal mid-plane of the rotor, the airflow angle of attack is slightly negative by a few degrees as compared with the flow unaltered by the presence of rotor. This

TABLE 3 Boundary conditions for turbulence variables

Boundary Patch	ν_t-BC	k-BC	ω-BC
Inlet	fixedValue	fixedValue	fixedValue
Outlet	zeroGradient	zeroGradient	zeroGradient
Side walls	zeroGradient	zeroGradient	zeroGradient
Device surface	nutUWallFunction	kqRWallFunction	omegaWallFunction

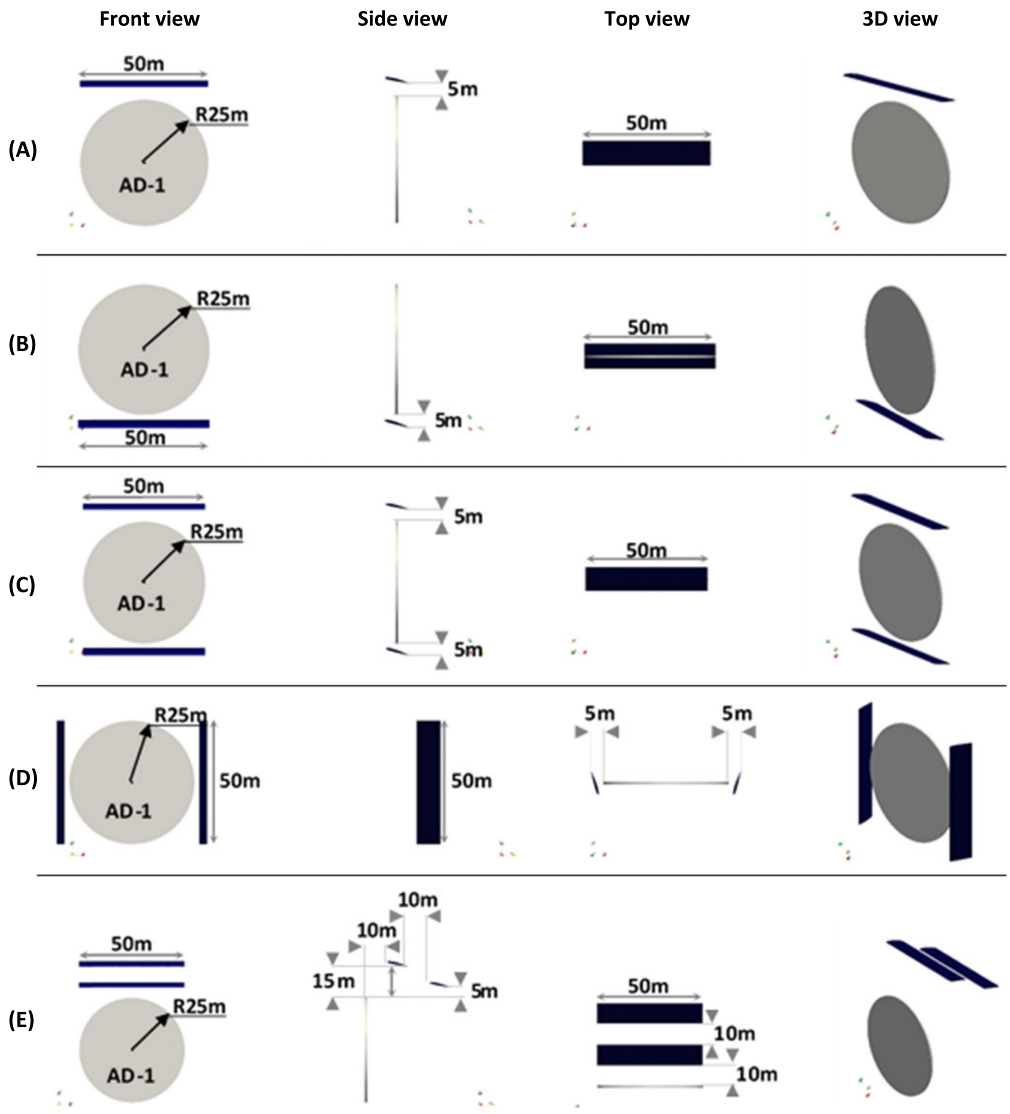

FIGURE 6 A-E: Geometry of devices 1 through 5. A, Device 1. B, Device 2. C Device 3. D, Device 4. E, Device 5. (Not to scale). F-J: Geometry of devices 6 through 10. F Device 6. G Device 7. H, Device 8. I Device 9. J Device 10. (Not to scale). Figure 6 is continued on the next page [Colour figure can be viewed at wileyonlinelibrary.com]

requires the parts of the device, lying above and below the horizontal mid-plane of the rotor, to be at different angles of attack. To prevent stalling, the ones lying above had to be placed at an angle of 13° with respect to the horizontal. The ones lying below did not stall until the angle with respect to the horizontal was increased to 17°. Despite the different angles of attack, both devices will have the same downward force (to first order) because they are operating at the same angle of attack compared with the incoming airflow.

4 | RESULTS

The results from the simulations are presented in this section. First, the results of all the cases (devices 1-10) with C_p = 0.45 and a turbine spacing of 3 rotor diameters are presented. As it will be shown that certain devices (6, 9, and 10) perform better than others, the turbine spacing (S) and the C_p are then varied only for the cases with better performing devices. For the sake of clarity, the structure and labeling of the different sets of simulations are summarized in Table 4.

Note that AD in the labeling of simulation sets stands for Actuator Disk. In all the simulations, the wake flow behind the upstream turbine (incident upon the plane of downstream rotor) is of interest. The key statistic used to quantify the performance (ie, the wake displacement and velocity recovery potential) of the devices is the dimensionless velocity deficit measured with respect to the wind speed at the inlet plane of upstream turbine and streamwise velocity at the plane of downstream rotor normalized using the unperturbed wind speed at the center of the disk-1. As the devices are located in the vicinity of the upstream rotor, it is important to note that their presence is felt by the upstream rotor via a modified pressure coefficient at the rotor exit plane. In some of the cases, the pressure coefficients at the exit plane of the upstream turbine

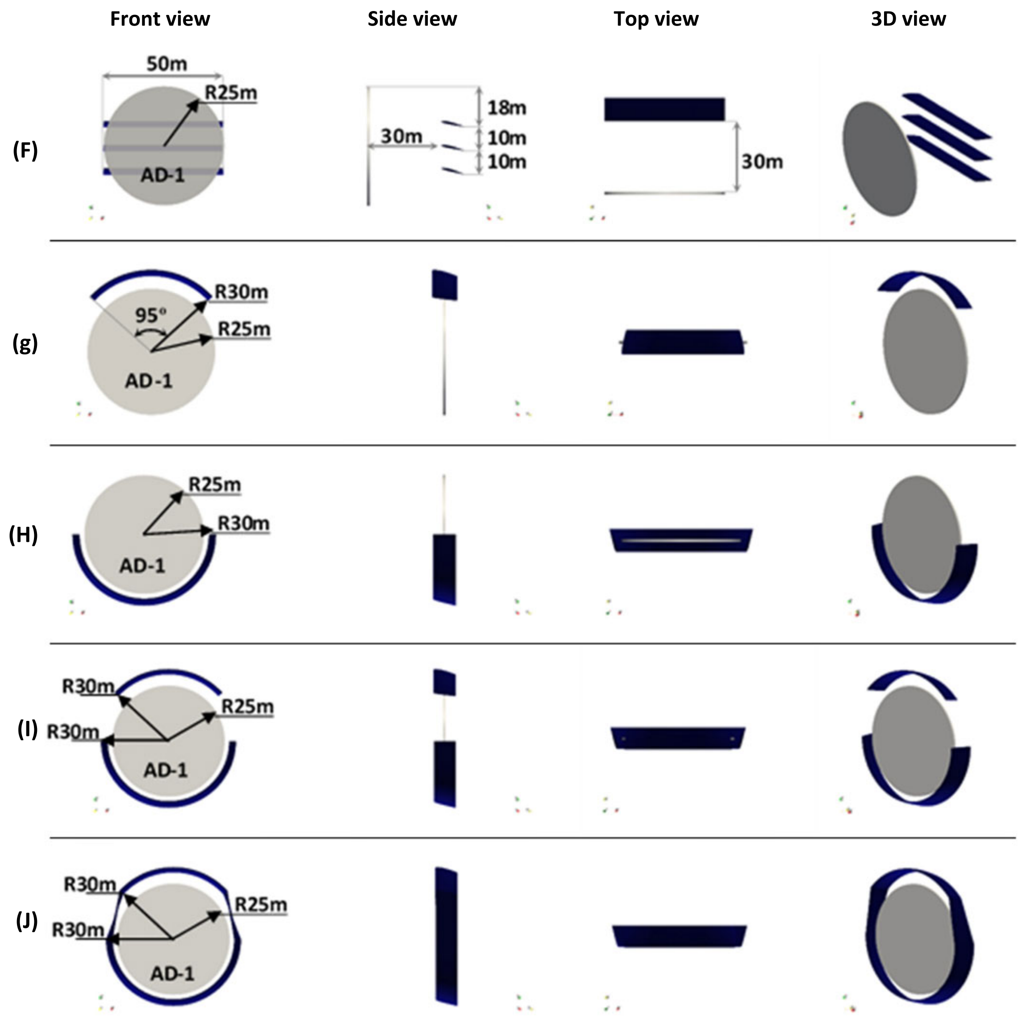

FIGURE 6 Continued.

TABLE 4 Labeling of simulation sets

Simulation Set	S	C_p
AD-I	3D	0.45
AD-II	3D	0.50
AD-III	6D	0.50

augmented with these devices become more negative, which in turn increases the mass flow rate of air passing through it, thereby also increasing the leading turbine's efficiency slightly. A brief quantification of the pressure coefficients at the exit plane of leading turbine is also considered in the analysis.

4.1 | Definition of coefficients and parameters

The metrics used to measure the performance of the devices proposed in this paper are described in this section. One of the most suitable ways to quantify the performance of the proposed devices is to measure their ability to recover the velocity in the wake. The velocity profile (as a function of x and z) at the inlet plane of the unmodified leading turbine is used as a reference value, U_{D1}. This ideally is what the downstream turbine would also measure but typically does not because the wake has less kinetic energy and velocity. The velocity profile at the inlet on the downstream turbine is then calculated as U_{D2}. The dimensionless, fractional velocity deficit (FVD) (plotted in Figures 8, 10, and 11) is then given by

$$\frac{\Delta U}{U_{D1}} = \frac{U_{D1} - U_{D2}}{U_{D1}}. \tag{10}$$

The values of FVD calculated in this manner include both the vertical and the spanwise effects of the wake flow. The FVD provides a simple yet informative estimate about the performance of the proposed devices.

Using U_{D1} and U_{D2}, the corresponding fluxes at the inlet planes of unmodified leading turbine and downstream turbine for different cases can be written as $\int U_{D1} dA_{rotor}$ and $\int U_{D2} dA_{rotor}$, respectively, where A_{rotor} is the blade plane area. Thus, we define the velocity deficit parameter (VDP) as follows:

$$VDP = \frac{\int U_{D1} dA_{rotor} - \int U_{D2} dA_{rotor}}{\int U_{D1} dA_{rotor}}. \tag{11}$$

The devices are primarily designed to improve the performance of the downstream turbine and not the upstream turbine they are usually mounted on. However, the device can also slightly affect the performance of the leading turbine as well. This can be measured by looking at the pressure coefficient. The measured pressure coefficient at the exit plane of the turbine is

$$\mathbb{C}_p = \frac{p - p_\infty}{\frac{1}{2}\rho U_\infty^2}, \tag{12}$$

where p is the integral of the exit pressure (static) over the rotor area computed behind the leading turbine, on a plane passing through the trailing edge of the device and whose normal points in the streamwise direction. p_∞ is the static pressure far upstream (1 atm) and U_∞ is the average streamwise velocity of the air far upstream. Note that, to avoid confusion with the nominal coefficient of performance C_p, of the turbine without any wake device nearby, the double struck capital "$\mathbb{C}_p$" has been used to denote the measured (or device modified) coefficient of pressure.

4.2 | AD-I simulation results

Figure 7 shows the contours of normalized streamwise velocity just ahead of rotor-2 (the downstream rotor of interest in this work). It is to be noted that the streamwise velocity of the unperturbed stream of air at the elevation of the centers of the disks, U_{ref} = 10 m/s, (yellow) has been

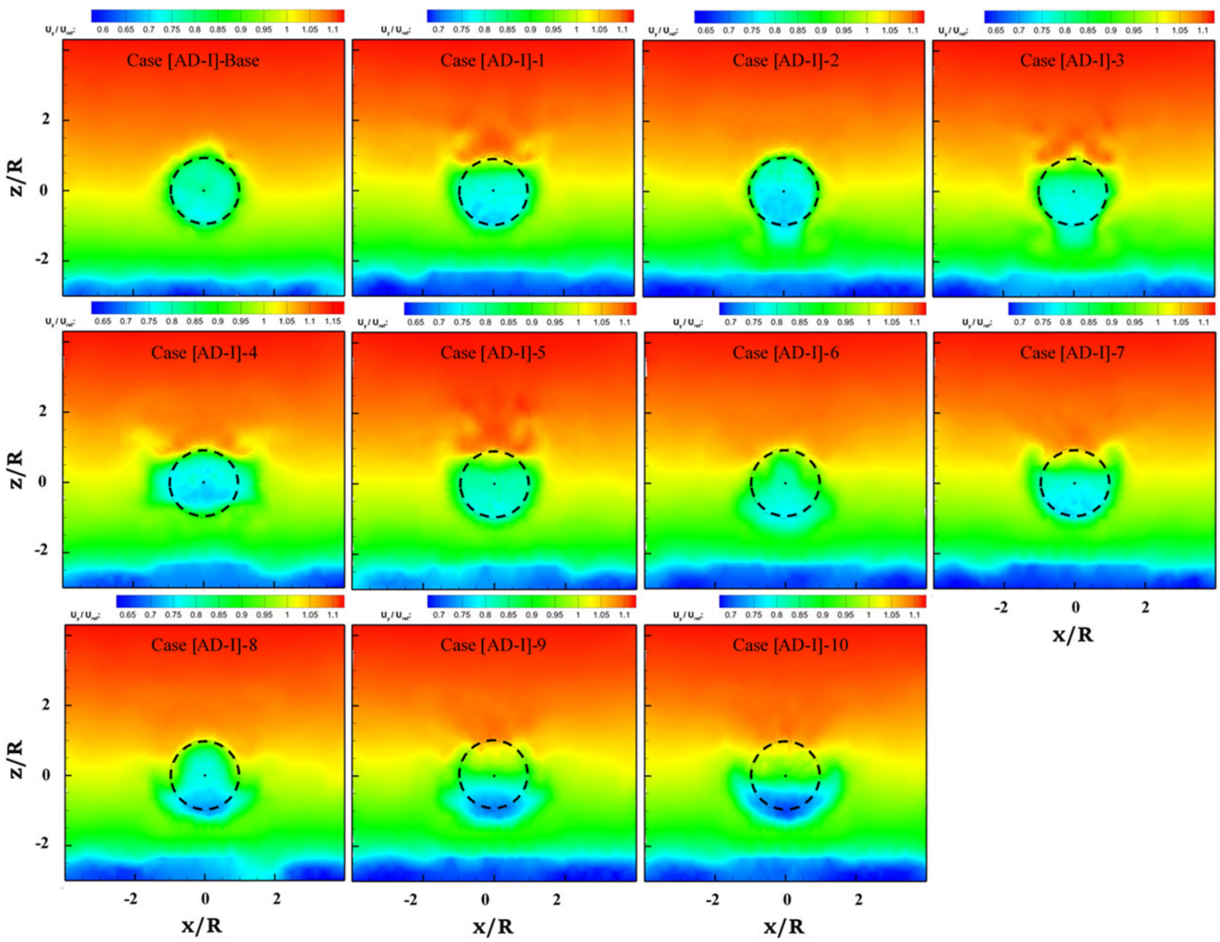

FIGURE 7 Normalized streamwise velocity $\left(\frac{U}{U_{ref}}\right)$ on a vertical plane just ahead of downstream rotor for AD-I simulations [Colour figure can be viewed at wileyonlinelibrary.com]

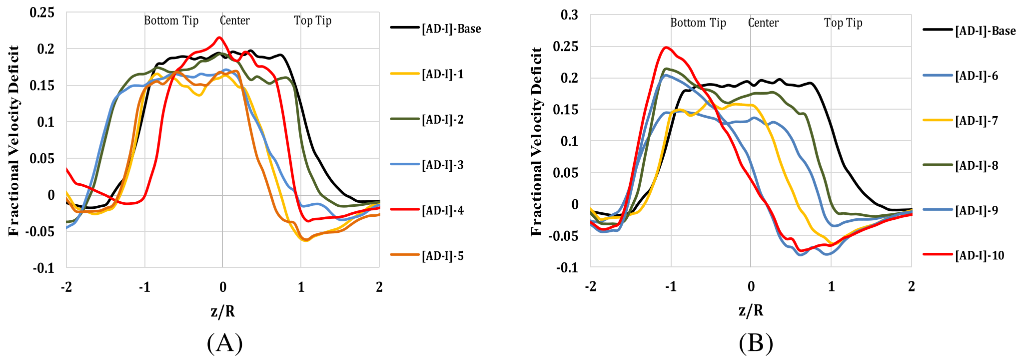

FIGURE 8 Wake displacement (downward) for AD-I simulations. A, Base and cases 1 through 5. B, Base and cases 6 through 10 [Colour figure can be viewed at wileyonlinelibrary.com]

used to normalize these plots. The black dot represents the disk center and the dashed circle represents the periphery of the disk-2 rotor. The displacement of the wake downwards with respect to the inlet area of disk-2 is clearly visible in these plots. The numbering (trailing numeral) of the cases follows from Section 3 where it represents the device, eg, Case [AD-I]-1 represents the case with the settings of set [AD-I] and with device 1. The "Base" case represents the case run without any device on the upstream turbine.

In Figure 8, the FVD (Equation (10)) is calculated on a vertical line (on the inlet plane of the downstream turbine) and is plotted for all the cases. This is equivalent to looking at the results of Figure 7 on vertical line through the middle of the turbine. The classic velocity deficit due to the wake is easily seen with the solid black line. At 3 diameters separation, the velocity is 20% less through the downstream turbine than through the first turbine. The percentage loss is almost constant even though the actual velocity across the rotor varies significantly from its bottom ($z/R = -1$) to its top ($z/R = 1$) due to the log-layer variation with height. This actual variation can be seen in Figure 7 but not in Figure 8, which has been normalized by the log-layer. The goal is to reduce this deficit to zero everywhere in the rotor (from $z/R = -1$ to 1). All the devices reduce the deficit near the top of the rotor ($z/R = 1$). And some of them even produce a velocity surplus (faster than normal velocity) at the top of the rotor. The devices do this by sucking fast air from above the top of the turbine, down into the rotor plane. The most effective devices can remove the deficit entirely even at the rotor center and only suffer some velocity deficit right at the bottom of the turbine. Any deficit below ($z/R = -1$) does not affect the second turbine's performance and is not a problem.

The values for the velocity deficit parameter are given in Table 5. These give a quantitative number for the qualitative evaluations of the devices in Figures 7 and 8. The base case shows an average velocity deficit of 16.5% for the base case with no device. Note that Figure 8 indicates 20% deficit for the base case but that is just on the centerline. The table evaluates the average for the entire rotor. A lower number is better with a value of zero (0) being full recovery of the velocity and total removal of the wake from the downstream turbine. The later designs, with the curved airfoils that reside as close as possible to the wake itself, tend to function better. However, one exception to this rule is design 6, which uses 3 flat airfoils directly behind the first turbine. This design is directly in the wake and has more airfoil surface area (and therefore net thrust) than the other designs. With more airfoils (or larger airfoils), the wake can always ultimately be moved away. The real goal of the designs is to move the wake without an inordinate amount of extra external structure to the design (hence, we usually use 1 or 2 airfoils of comparable size to the turbine itself). Table 5 also shows the coefficients of pressure defined previously in Section 4.1 and Equation (12). Values that are more negative than the base case indicate an improvement in the performance of the leading turbine. The entire periphery along the trailing edge of some devices (designed to push the flow away from the rotor axis), mimics the diffuser shrouds, resulting in a low-pressure region behind the

TABLE 5 Velocity deficit parameter and leading turbine exit pressure coefficient for [AD-I] simulations

Case	VDP	C_p
[AD-I]-base	0.165	−0.133
[AD-I]-1	0.114	−0.064
[AD-I]-2	0.145	−0.206
[AD-I]-3	0.116	−0.142
[AD-I]-4	0.144	−0.319
[AD-I]-5	0.113	−0.070
[AD-I]-6	0.074	−0.127
[AD-I]-7	0.089	−0.040
[AD-I]-8	0.111	−0.359
[AD-I]-9	0.046	−0.245
[AD-I]-10	0.041	−0.350

Abbreviation: VDP, velocity deficit parameter.

leading turbine, thereby admitting more wind through the rotor. The large, negative values of pressure coefficient for the cases with vertical airfoils [AD-I]-4, lower curved airfoil [AD-I]-8 and the Wind Ring [AD-I]-10 attest to this, as all these 3 devices push the flow out (downwards and sideways).

In Table 6, the normalized power available at the upstream and downstream rotors is presented. P_{D1} and P_{D2} are the power available in the wind at rotors 1 and 2, respectively. The power available in the wind in the base case for each disk (P_{B1} and P_{B2}) has been used to normalize the power for each case. The last column shows the total normalized power of the wind farm (both turbines). The power available in the wind is very sensitive to the velocity (because of the cubic relationship). Some of the devices (1, 5, and 7) slightly reduce the performance of the upstream turbine that they are near and show a value in the first column that is less than 1. But some of the other devices actually enhance the performance of the upstream turbine and the downstream turbine (which was the intended target). They do this because they also inadvertently can act like diffusers as explained in the previous paragraph. A good example of this effect is design 4 (the vertical airfoils on the rotor sides). This design improves the performance of the upstream turbine (by 36 %) but has little ability to move the wake away and does little for the downstream turbine. Design 8 is actually similar in its behavior. It is a better upstream turbine diffuser than it is a wake mover. Design 6 (the 3 airfoils behind) is roughly the opposite. Because it is downstream, it has almost no effect on the upstream turbine (it is too far downstream). And all its effect is on the downstream turbine.

Some of the designs, like the last 2, do both. They act like a diffuser improving the upstream turbine power considerably and moving the wake away from the downstream turbine. The final column shows that these devices (on only the upstream turbine) can increase the wind farm power by 60%. Power increase could be even larger if these devices were installed on the downstream turbines as well. All designs improve the farm power. But in designs 1, 5, and 7, the loss in performance of the upstream turbine is only barely compensated for by the improved performance of the downstream turbine for total power increase in the farm of only 3% or less.

4.3 | AD-II and AD-III results

Figure 9 shows the contours of normalized streamwise velocity just ahead of rotor-2 for [AD-II] (higher C_p base turbines) and [AD-III] (higher C_p and double the turbine separation) simulations. As mentioned before, U_{ref} = 10 m/s, has been used to normalize these plots. The black dot represents disk center and the dashed circle represents the periphery of the disk-2. These simulations focus on design 6 (3 trailing airfoils) because of the simplicity of the design and effectiveness at moving the wake and designs 9 and 10 (the open and closed rings).

When the turbine efficiency is increased (cases AD-II), the turbine's ability to extract energy is increased, but the results remain largely the same as Figure 7. The blues are darker because the wake is even slower for these turbines. But the ability to move the wake remains almost identical. This means the wake moving device performance is not sensitive to the actual design of the turbine it is attached to.

The AD-III cases (lower row), which look at what happens when we have a larger spacing, are more interesting. These cases are identical to the row above them (same C_p) except have twice the distance to move the wake away. And at these separations (6 diameters), the devices entirely remove the wake from the downstream turbine. It can be seen that they even pull high speed air down into the second turbine, which will increase its performance.

Figures 10 and 11 show the effect on the wake deficit for AD-II and AD-III. Again, Figure 10 looks like Figure 8 in almost all aspects, except the base case shows a velocity deficit of 25% now (rather than 20% for the AD-I simulations). The strength of the wake does not affect, positively or negatively, our ability to move the wake. However, Figure 11 shows that with twice the separation, the device can move down the point of minimum velocity in the wake further downwards. This means the best devices move the wake almost entirely away from the rotor disk (below $z/R < -1$).

Tables 7 and 8 show the velocity deficit parameter. The values found are very comparable to Table 5. Changing the turbine base efficiency (C_p) does not change the devices ability to move the wake. At this separation the devices almost recover the velocity (a value of 0) but not completely.

TABLE 6 Normalized power for [AD-I] simulations

Case	$\frac{P_{D1}}{P_{B1}}$	$\frac{P_{D2}}{P_{B2}}$	$\frac{P_{D,Total}}{P_{B,Total}}$
[AD-I]-1	0.935	1.143	1.014
[AD-I]-2	1.219	1.039	1.151
[AD-I]-3	1.138	1.142	1.139
[AD-I]-4	1.361	1.047	1.242
[AD-I]-5	0.964	1.143	1.032
[AD-I]-6	1.002	1.293	1.112
[AD-I]-7	0.908	1.237	1.032
[AD-I]-8	1.950	1.156	1.650
[AD-I]-9	1.758	1.385	1.617
[AD-I]-10	1.709	1.404	1.594

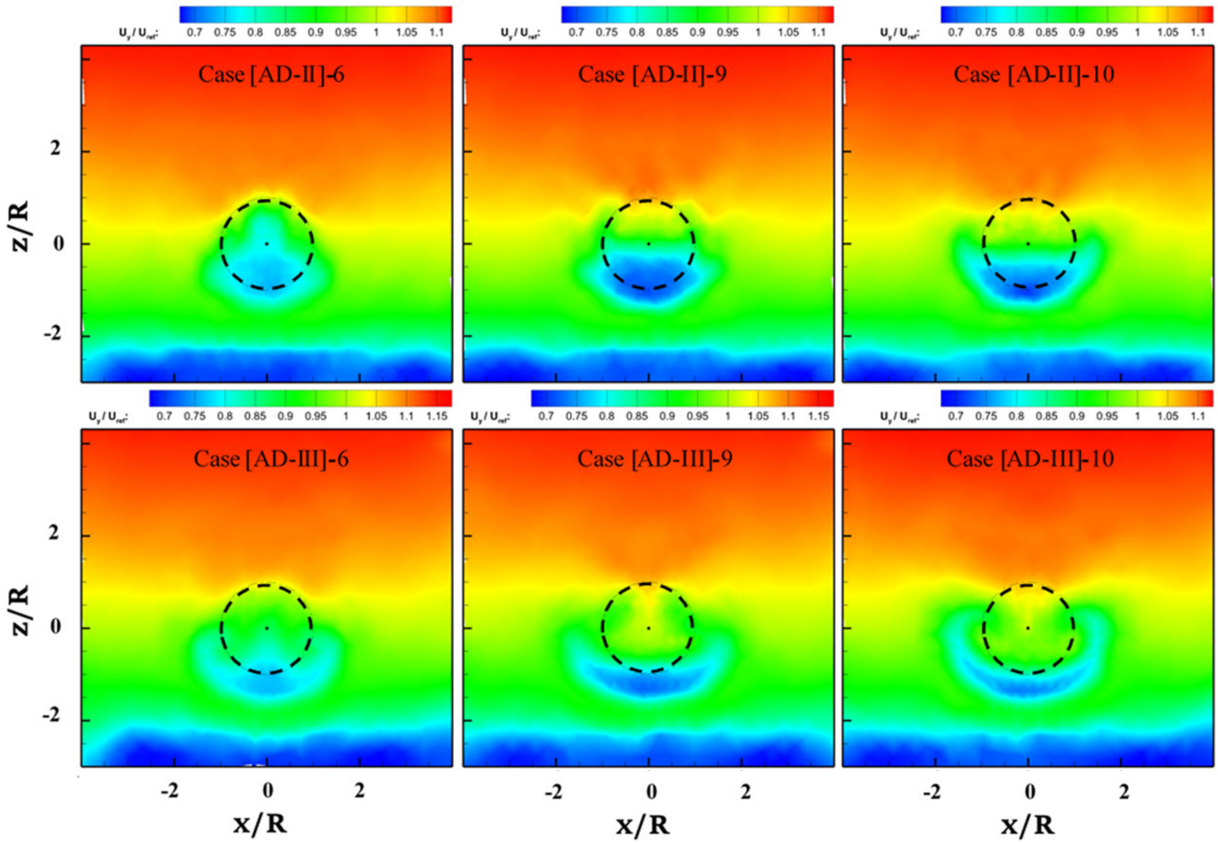

FIGURE 9 Normalized streamwise velocity $\left(\frac{U}{U_{ref}}\right)$ on a vertical plane just ahead of downstream rotor for AD-II and AD-III simulations [Colour figure can be viewed at wileyonlinelibrary.com]

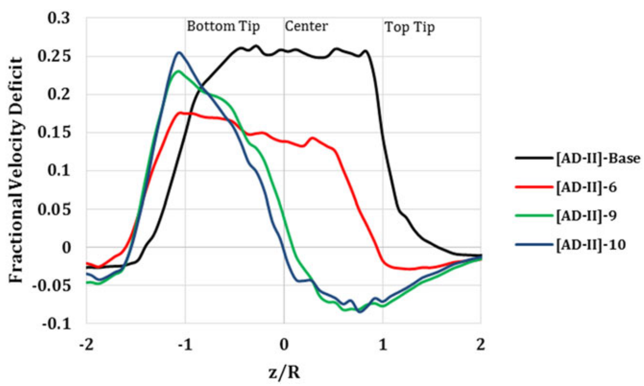

FIGURE 10 Wake displacement for AD-II simulations [Colour figure can be viewed at wileyonlinelibrary.com]

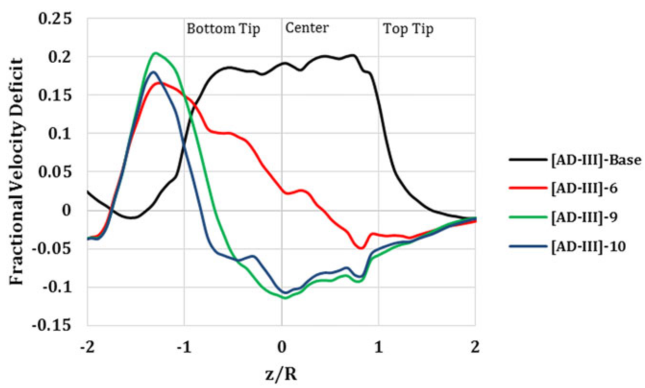

FIGURE 11 Wake displacement for AD-III simulations [Colour figure can be viewed at wileyonlinelibrary.com]

TABLE 7 Velocity deficit parameter for cases [AD-II]-6, 9, and 10

Case	VDP
[AD-II]-6	0.088
[AD-II]-9	0.054
[AD-II]-10	0.028

Abbreviation: VDP, velocity deficit parameter.

TABLE 8 Velocity deficit parameter for cases [AD-III]-6, 9, and 10

Case	VDP
[AD-III]-6	0.023
[AD-III]-9	−0.033
[AD-III]-10	−0.043

Abbreviation: VDP, velocity deficit parameter.

TABLE 9 Normalized power for cases [AD-II]-6, 9, and 10

Case	$\frac{P_{D1}}{P_{B1}}$	$\frac{P_{D2}}{P_{B2}}$	$\frac{P_{D,Total}}{P_{B,Total}}$
[AD-II]-6	1.016	1.558	1.191
[AD-II]-9	1.741	1.706	1.729
[AD-II]-10	1.775	1.835	1.795

TABLE 10 Normalized power for cases [AD-III]-6, 9, and 10

Case	$\frac{P_{D1}}{P_{B1}}$	$\frac{P_{D2}}{P_{B2}}$	$\frac{P_{D,Total}}{P_{B,Total}}$
[AD-III]-6	0.993	1.529	1.192
[AD-III]-9	1.650	1.777	1.697
[AD-III]-10	1.715	1.840	1.762

On the other hand, Table 8 shows that for the best 2 devices (the rings) the downstream turbines can have negative velocity deficits. This means that they have (3% to 4%) faster air entering them than if there was no turbine ahead of them at all. The device has not only entirely removed the wake at this extra separation, they have also entrained some fast high altitude air.

Tables 9 and 10 look at the power increase in the first, second, and total farm. Design 6 still does a good job at moving the wake away and thereby increasing the performance of the downstream turbine (as intended). But the 2 rings enhance the power in both turbines leading to 70-80% power enhancement for the combined farm. Increasing the separation does not increase the power of the farm (and shows a slight decrease) because the base power in AD-III is larger than case AD-II already. The larger separation reduces the wake deficit and the wake loss effect in the base case.

5 | CONCLUSIONS

In this paper, we have discussed a novel approach to remove the inefficiency caused by wind turbine wakes. The working principle of the devices proposed in this work is their ability to displace the wake of the upstream turbine out of the way of downstream turbine. To ensure the least drag and kinetic energy loss due to the proposed devices themselves, we have based our designs on airfoils.

The results presented in this paper are derived from the RANS simulations of the flow around 2 wind turbines placed in a turbulent atmospheric boundary layer. We have used the k/ω-SST turbulence model for the closure of the RANS equations. The modeling of the wind turbines was performed by using one of the simplest models to simulate the wind turbine wake, namely, the actuator disk model, which adds a source of forcing (drag) opposite to the flow within the volume swept by the turbine rotor blades.

The performance of the proposed devices depends significantly on the device airfoil's position relative to the leading turbine. Many of the proposed devices contain 2 parts- one airfoil, which is placed below the turbine rotor to deflect the slow air in the lower layers of the ABL further downwards and sideways, and one airfoil which is placed above the actuator disk to entrain faster air from the upper layers of ABL. The lower airfoil pulls the wake downwards and the upper airfoil pushes the wake downward. The more force downwards the quicker the wake moves. This basic principle was directly tested with 1-airfoil, 2-airfoil, and even one 3-airfoil design.

From the simulation results, it was shown that devices with curved airfoils, namely, device 9, which consists of 2 nonjoined curved airfoils aligned along the periphery of the leading turbine and device 10 in which the 2 curved airfoils are joined together to form a closed-ring-like structure, are found to be most effective. Design 6 (3 airfoils placed in the wake almost 1-rotor radius behind the leading turbine) was attractive for its simplicity and showed an ability to move the wake. But 9 and 10 also enhanced the power of the leading turbine. In the set of simulations with the interturbine spacing of 6 rotor diameters (AD-III), devices 9 and 10 demonstrated the ability to recover all of the velocity deficit in the wake as well as the ability to even enhance the average wake velocity in the downstream turbine. They also achieved this performance improvement in the downstream turbine while enhancing the performance of the upstream turbine they were attached to.

ACKNOWLEDGEMENT

The third author was supported in part by the National Science Foundation grants 1353942 and 1336502. A provisional patent (docket number 3724.037PRV) for these designs was granted in July 2017.

ORCID

J. B. Perot http://orcid.org/0000-0002-3279-1981

REFERENCES

1. Short W, Blair N, "20% wind energy by 2030: increasing wind energy's contribution to US electricity supply," DOE Report No. DOfJGO-102008-2567, 2008.
2. Barthelmie RJ, Hansen K, Frandsen ST, et al. Modelling and measuring flow and wind turbine wakes in large wind farms offshore. *Wind Energ*. 2009;12(5):431-444. https://doi.org/10.1002/we.348
3. Schottler J, Mühle F, Bartl J, et al. Comparative study on the wake deflection behind yawed wind turbine models. *J Phys Conf Ser*. 2017;854:012032. https://doi.org/10.1088/1742-6596/854/1/012032
4. Adaramola MS, Krogstad PÅ. Experimental investigation of wake effects on wind turbine performance. *Renew Energy*. 2011;36(8):2078-2086. https://doi.org/10.1016/j.renene.2011.01.024
5. Jiménez Á, Crespo A, Migoya E. Application of a LES technique to characterize the wake deflection of a wind turbine in yaw. *Wind Energ*. 2010;13:559-572. https://doi.org/10.1002/we.380
6. Vollmer L, Steinfeld G, Heinemann D, Kühn M. Estimating the wake deflection downstream of a wind turbine in different atmospheric stabilities: an LES study. *Wind Energ Sci*. 2016;1(2):129-141. https://doi.org/10.5194/wes-1-129-2016
7. Gebraad PMO, Teeuwisse FW, van Wingerden JW, et al. Wind plant power optimization through yaw control using a parametric model for wake effects—a CFD simulation study. *Wind Energ*. 2016;19(1):95-114. https://doi.org/10.1002/we.1822
8. Gebraad P, Thomas JJ, Ning A, Fleming P, Dykes K. Maximization of the annual energy production of wind power plants by optimization of layout and yaw-based wake control. *Wind Energ*. 2017;20(1):97-107. https://doi.org/10.1002/we.1993
9. Cal RB, Lebrón J, Castillo L, Kang HS, Meneveau C. Experimental study of the horizontally averaged flow structure in a model wind-turbine array boundary layer. *J Renew Sustain Ener*. 2010;2(1):013106. https://doi.org/10.1063/1.3289735
10. Calaf M, Meneveau C, Meyers J. Large eddy simulation study of fully developed wind-turbine array boundary layers. *Phys Fluids*. 2010;22(1):015110. https://doi.org/10.1063/1.3291077
11. VerHulst C, Charles Meneveau C. Altering kinetic energy entrainment in large eddy simulations of large wind farms using unconventional wind turbine actuator forcing. *Energies*. 2015;8(1):370-386. https://doi.org/10.3390/en8010370
12. Ploumakis E. Improving the Wind Farm efficiency by simple means. 2016. https://repository.tudelft.nl/islandora/object/uuid: a273b26a-b4bd-4388-8eee-193c6d22626b?collection=education
13. Gilbert BL, Oman RA, Foreman KM. Fluid dynamics of diffuser-augmented wind turbines. *J Energy*. 1978;2(6):368-374. https://doi.org/10.2514/3.47988
14. Phillips DG, Flay RGJ, Nash TA. Aerodynamic analysis and monitoring of the Vortec-7 diffuser-augmented wind turbine. *Transactions of the Institution of Professional Engineers New Zealand: Electrical/Mechanical/Chemical Engineering Section*. 1999;26(1):13-19. https://www.researchgate.net/profile/Richard_Flay/publication/237454837_Aerodynamic_analysis_and_monitoring_of_the_Vortec_7_Diffuser-Augmented_wind_turbine/links/02e7e52d87a1b70581000000/Aerodynamic-analysis-and-monitoring-of-the-Vortec-7-Diffuser-Augmented-wind-turbine.pdf
15. Abe K, Nishida M, Sakurai A, et al. Experimental and numerical investigations of flow fields behind a small wind turbine with a flanged diffuser. *J Wind Eng Ind Aerod*. 2005;93(12):951-970. https://doi.org/10.1016/j.jweia.2005.09.003
16. Ohya Y, Karasudani T. A shrouded wind turbine generating high output power with wind-lens technology. *Energies*. 2010;3(4):634-649. https://doi.org/10.3390/en3040634
17. Versteeg HK, Malalasekera W. An introduction to computational fluid dynamics: the finite volume method. *Pearson Education*. 2007.
18. OpenFOAM (2011). User Guide. http://www.openfoam.org/docs/user/index.php.
19. Song Y, Perot JB. CFD simulation of the NREL phase VI rotor. *Wind Engineering*. 2015;39(3):299-310. https://doi.org/10.1260/0309-524X.39.3.299
20. Patankar S. *Numerical Heat Transfer and Fluid Flow*. CRC press; 1980.
21. Manwell JF, McGowan JG, Rogers AL. *Wind Energy Explained: Theory, Design and Application*. John Wiley & Sons; 2010.

22. Gomes VC, Palma JM, Lopes AS. Improving actuator disk wake model. *J Phys Conf Ser*. 2014;524(1):012170. https://doi.org/10.1088/1742-6596/524/1/012170
23. ANSYS, Inc. https://www.ansys.com/
24. Anderson D, Tannehill JC, Pletcher RH. *Computational Fluid Mechanics and Heat Transfer*. 3rd ed. CRC Press; 2012.
25. Menter FR. Two-equation eddy-viscosity turbulence models for engineering applications. *AIAA Journal*. 1994;32(8):1598-1605. https://doi.org/10.2514/3.12149
26. Perot JB. Turbulence modeling using body force potentials. *Phys Fluids*. 1999;11(9):2645-2656. https://doi.org/10.1063/1.870126
27. OpenFOAM Extended Code Guide (2016). http://www.openfoam.com/documentation/cpp-guide/
28. Menter FR, Kuntz M, Langtry R. Ten years of industrial experience with the SST turbulence model. *Proceedings of the fourth international symposium on turbulence, heat and mass transfer*, pages 625–632, Antalya, Turkey, 2003. Begell House.
29. UIUC Airfoil Coordinates Database, UIUC Applied Aerodynamics Group, http://m-selig.ae.illinois.edu/ads/coord_database.html

How to cite this article: Bader S, Inguva V, Perot JB. Improving the efficiency of wind farms via wake manipulation. *Wind Energy*. 2018;1–15. https://doi.org/10.1002/we.2226